Supplementary Information

Covalent-assisted seeding of Si nanoparticles into a dual-matrix design toward advanced Si-based Li-ion batteries

*Kwanghyun Do[a], Changyong Park[af], Jeonguk Hwang[a], Sucheol Kim[ab], Yeju Jung[a], Se Hun Lee[c], Hee-Dae Lim[*df], Heejoon Ahn[*abef]*

[a]Department of Organic and Nano Engineering, Hanyang University, 222 Wangsimni-ro, Seongdong-gu, Seoul, 04763, Republic of Korea

[b]Human-Tech Convergence Program, Department of Organic and Nano Engineering, Hanyang University, 222 Wangsimni-ro, Seongdong-gu, Seoul, 04763, Republic of Korea

[c]Advanced Institutes of Convergence Technology, Seoul National University, Suwon, Gyeonggi-do, 16229, Republic of Korea

[d]Department of Chemical Engineering, Hanyang University, 222 Wangsimni-ro, Seongdong-gu, Seoul, 04763, Republic of Korea

[e]Department of Battery Engineering, Hanyang University, 222 Wangsimni-ro, S`eongdong-gu, Seoul, 04763, Republic of Korea

[f]Institute of Nano Science and Technology, Hanyang University, 222 Wangsimni-ro, Seongdong-gu, Seoul, 04763, Republic of Korea

**Corresponding author: E-mail: ahn@hanyang.ac.kr (Heejoon Ahn), hdlim@hanyang.ac.kr (Hee-Dae Lim)*

Reaction mechanisms of silicon alkoxides under acidic or basic conditions

Due to the limited water solubility of most silicon alkoxides, alcohols were employed as co-solvents to ensure thorough mixing of the reactants and to promote the reaction. The sol-gel chemistry, depicted in Eq. (1), may appear straightforward, but it is quite complex due to the competing hydrolysis and condensation reactions, which are influenced by several factors, including the precursor type, solvent, alkoxy group-to-water ratio, catalyst, pH, and temperature, *etc*. The structural evolution of polyvinylsilsesquioxane (PVSQ) produced from vinyltriethoxysilane (VTES) is influenced by several factors. Among these factors, pH is the most important as it controls the morphology of the final product by influencing the relative rates of hydrolysis and condensation of silicon alkoxide. Under acidic conditions, PVSQ forms chain-like networks because the hydrolysis and condensation reactions at terminal silicon atoms (atoms with zero or one Si−O−Si bond) possessing high electron density. Conversely, under basic conditions, PVSQ forms more branched and highly condensed networks due to the preference for reactions at central silicon atoms (atoms with two or three Si−O−Si bonds) with low electron density. This structural difference is based on the inductive effects of the substituents attached to the silicon atom and the degree of stabilization of the transition states during the hydrolysis and condensation reactions at a certain pH [1-3]. Based on these principles, pH was selected as the decisive parameter for Si@SiOC complexation.

Supporting Tables

Sample	Si NPs [g]	VTES [mol]	Reaction time [hrs]	Si NPs-seeded PVSQ network [g]	Yield of ceramization [%]	Si NPs content [wt.%]
Si0.1@SiOC	0.1 g	0.05	6	1.21	91.2	9.1
Si0.3@SiOC	0.3 g	0.05	6	2.19	92.1	14.9
Si0.5@SiOC	0.5 g	0.05	6	2.35	93.2	22.8
Si1.0@SiOC	1 g	0.05	6	2.78	93.8	35.5
Si1.5@SiOC	1.5 g	0.05	6	3.42	95.5	45.9

Table S1. Quantitative summary of Si_x@SiOC synthesis.

In the Si@SiOC system (Table S1), the concentration of VTES, temperature, and reaction time remained constant, whereas the amount of Si nanoparticles (NPs) varied from 0.1 to 1.5 g. The Si NP content (wt.%) represents the weight percentage of Si NPs injected in $Si_{0.1}$@SiOC, $Si_{0.3}$@SiOC, $Si_{0.5}$@SiOC, $Si_{1.0}$@SiOC, and $Si_{1.5}$@SiOC, respectively, before the sol-gel reaction into the final composite after pyrolysis. This value was estimated by assuming that no weight loss occurred for the Si NPs during washing or pyrolysis. The ceramization yield (%) indicates the percentage of weight of the composite before and after pyrolysis, and tends to decrease as the relative ratio of PVSQ in the composite increases. The decrease is ascribed to depolymerization and redistribution of the Si−O−C network that occurs when the pre-ceramic polymer is converted into SiOC.

Table S2. Quantitative summary of $SiSn_x$@SiOC synthesis.

Sample	Si NPs [g]	VTES [mol]	$SnCl_2 \cdot H_2O$ [mmol]	Reaction time [hrs]	Si NPs@ $Sn_3O_2(OH)_2$@ PVSQ network [g]	Yield of ceramization [%]	Si NPs content [wt.%]	Sn content [wt.%]
Si@SiOC	0.5	0.05	-	6	2.35	93.2	22.8	-
$SiSn_{0.2}$@SiOC	0.5	0.05	0.2	6	2.46	92.0	22.1	0.33
$SiSn_{1.0}$@SiOC	0.5	0.05	1	6	2.41	89.6	23.2	1.57
$SiSn_{2.0}$@SiOC	0.5	0.05	2	6	2.48	89.4	22.4	2.17

In the SiSn@SiOC system (Table S2), the amount of Si NPs was fixed at 0.5 g, and the amount of tin chloride dihydrate was controlled from 0.2 to 2 mmol. The Si NP content (wt.%) was carefully controlled to achieve similar values of approximately 22.1−23.2, while the metallic Sn content (wt.%) increased from 0.33 to 2.17 as the quantity of injected tin chloride increased.

Table S3. Fitting results from the Nyquist plots using the equivalent circuit for Si_x@SiOC and $SiSn_x$@SiOC electrodes after formation, 100, and 200 cycles

Sample	After formation cycles			After 100 cycles			After 200 cycles		
	R_o [ohm]	R_{SEI} [ohm]	R_{CT} [ohm]	R_o [ohm]	R_{SEI} [ohm]	R_{CT} [ohm]	R_o [ohm]	R_{SEI} [ohm]	R_{CT} [ohm]
$Si_{0.1}$@SiOC	2.3	2.1	10.6	3.0	2.4	16.7	-	-	-
$Si_{0.5}$@SiOC (Si@SiOC)	2.0	2.3	19.4	4.3	2.9	16.8	9.7	11.0	33.6
$Si_{1.5}$@SiOC	2.6	1.2	28.8	5.9	26.1	30.8	-	-	-
$SiSn_{1.0}$@SiOC (SiSn@SiOC)	1.9	1.9	12.1	3.8	2.0	8.6	9.4	7.6	11.1
$SiSn_{2.0}$@SiOC	2.1	1.9	11.2	4.9	2.7	10.3	8.5	7.6	15.7

Supporting Figures S1-S14

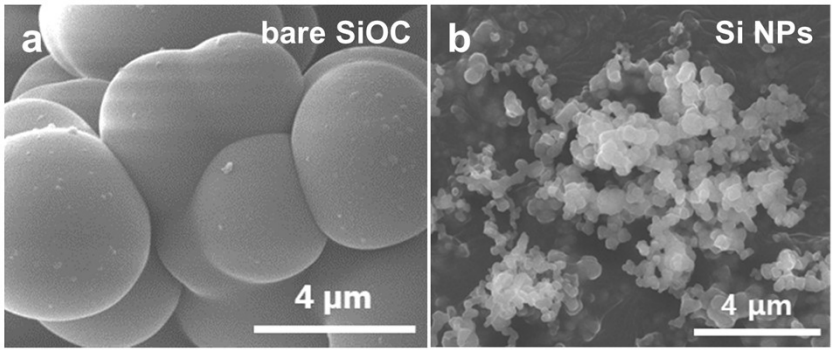

Fig. S1. Powder SEM images of (a) bare SiOC and (b) Si NPs.

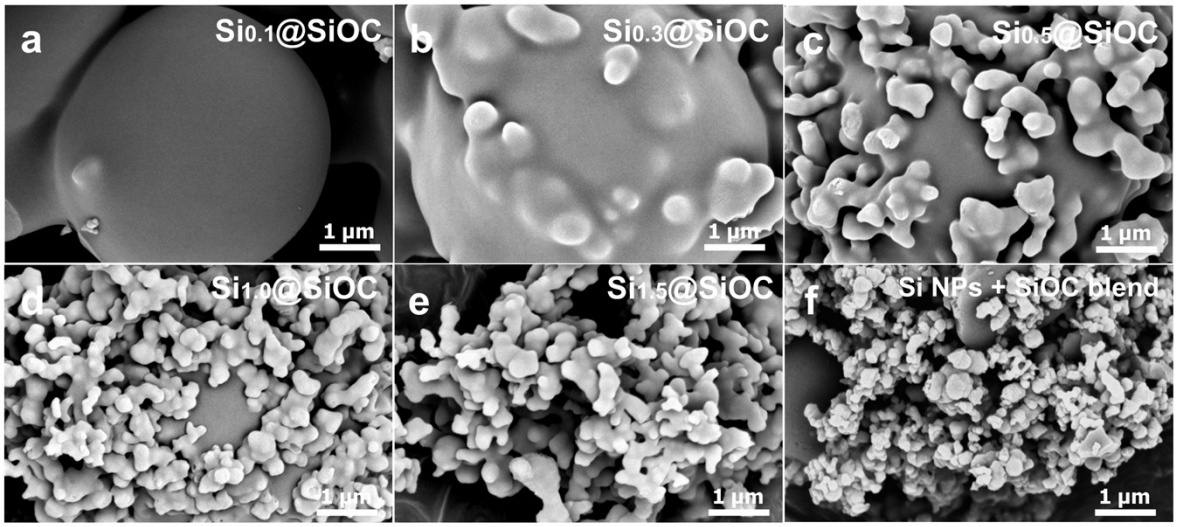

Fig. S2. Powder SEM images of (a) $Si_{0.1}$@SiOC, (b) $Si_{0.3}$@SiOC, (c) $Si_{0.5}$@SiOC, (d) $Si_{1.0}$@SiOC, (e) $Si_{1.5}$@SiOC, and (f) a physical blend of Si NPs and bare SiOC.

In **Fig. 1c** and **Fig. S2**, the SEM images were obtained at a voltage (5 kV) lower than the typical accelerating voltage (15 kV). Using a lower accelerating voltage allows surface-sensitive images to be obtained by minimizing issues such as charging, contamination, and beam damage, which may occur at high voltages. Therefore, we selected a low voltage to observe whether SiOC covered the surface of the Si NPs as the Si NPs content increased. The size of bare SiOC synthesized from VTES without Si NPs is approximately 2−5 um (**Fig. S2a**), and the size of bare Si NPs is approximately 100−200 nm (**Fig. S2b**).

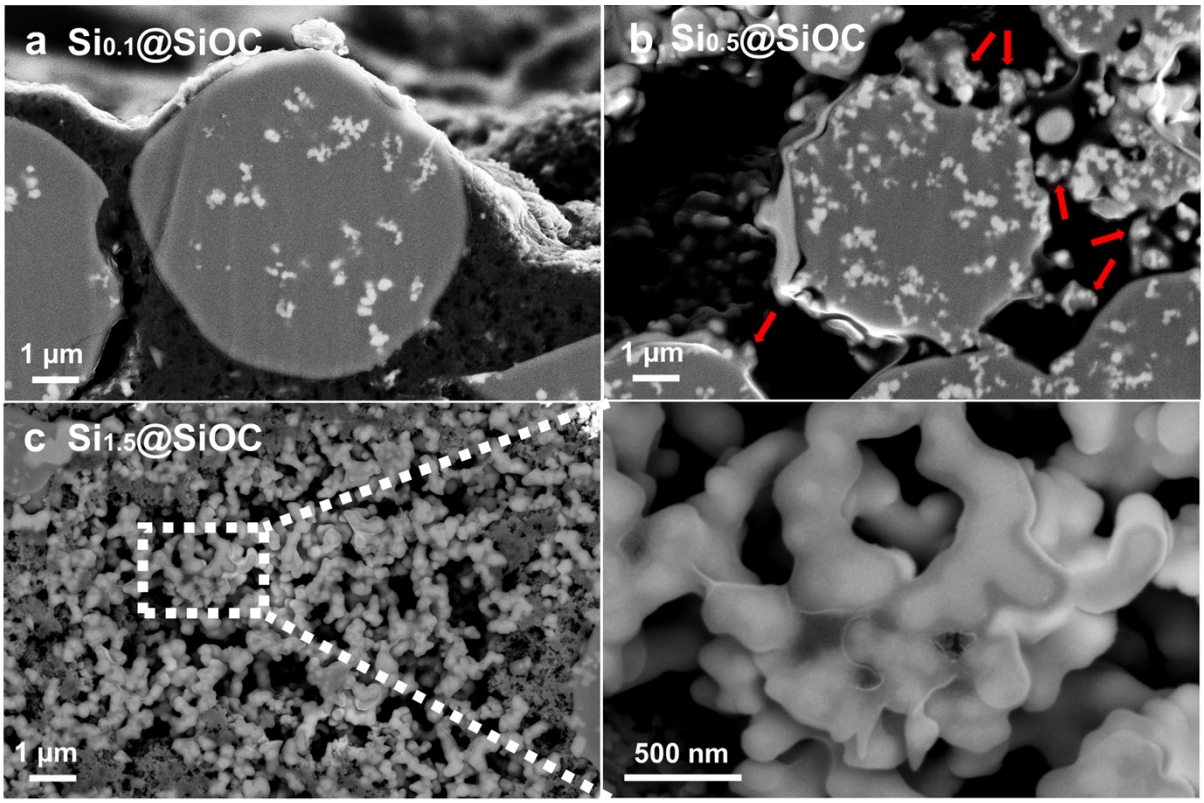

Fig. S3. Cross-sectional SEM images of (a) $Si_{0.1}$@SiOC, (b) $Si_{0.5}$@SiOC, and (c) $Si_{1.5}$@SiOC electrodes.

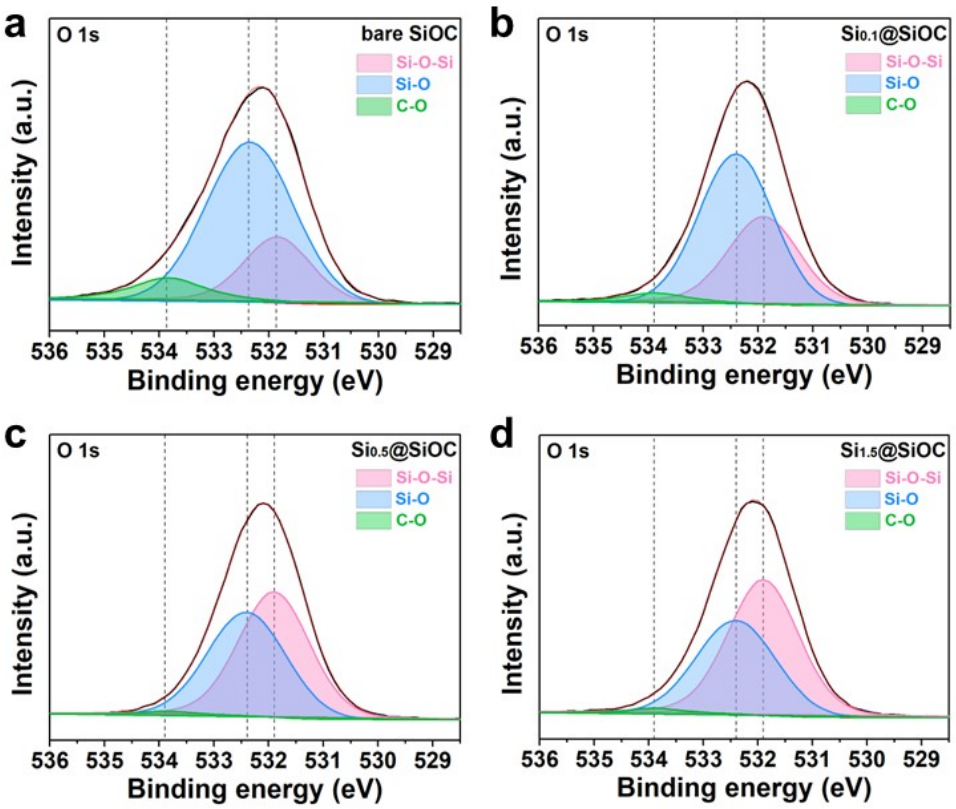

Fig. S4. XPS O 1s spectrum of (a) bare SiOC, (b) $Si_{0.1}$@SiOC, (c) $Si_{0.5}$@SiOC, and (d) $Si_{1.5}$@SiOC powders.

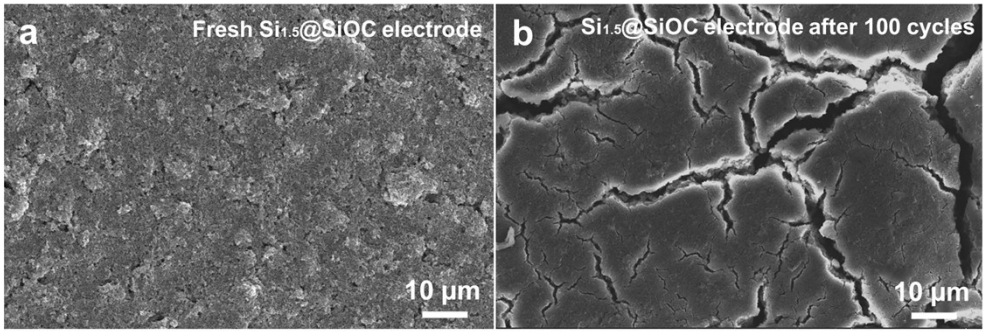

Fig. S5. Cross-sectional SEM images of $Si_{1.5}$@SiOC electrode (a) before and (b) after 100 cycles.

During charge/discharge, the $Si_{1.5}$@SiOC electrode could not withstand the intense mechanical stress owing to the high Si NP content, and the particles collapsed, resulting in a very thick SEI layer.

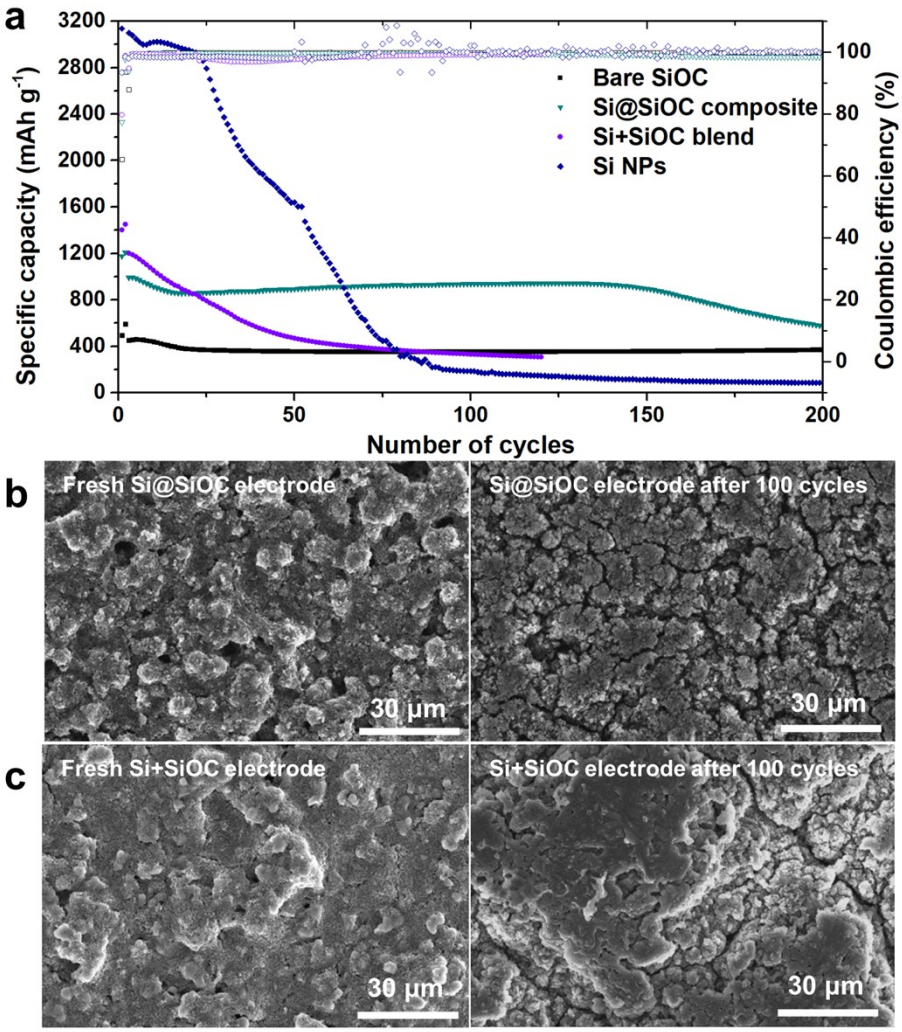

Fig. S6. (a) Cycle stability of bare SiOC, Si@SiOC, Si+SiOC blend, and Si NP electrodes. SEM images of (b) Si@SiOC and (c) Si+SiOC blend electrodes before and after 100 cycles.

To confirm the effect of the CAS Si-NPs, an electrode was fabricated by physically mixing bare SiOC and Si NPs with the same content as $Si_{0.5}$@SiOC (22.8 wt.%). **Fig. S6a** compares the cycle stability of the electrode composed of the CAS-driven Si@SiOC composite ($Si_{0.5}$@SiOC) and the electrode fabricated by simply blending bare SiOC and Si NPs. The capacity decayed much faster in the blended electrode than in the CAS-driven composite electrode. **Fig. S6b and c** show the SEM images of the Si@SiOC and blended electrodes before and after 100 cycles. The Si@SiOC composite, in which Si NPs were embedded inside the SiOC via covalent bonding, maintained its integrity after 100 cycles (**Fig. S6b**). However, in the Si+ SiOC-blended electrode, where the surfaces of the Si NPs are exposed, SEI propagation mainly occurs from the exposed Si NPs during the cycle, thereby damaging the integrity of the electrode (**Fig. S6c**). These results highlight the necessity of using CAS-driven Si@SiOC composites for advanced LIB anode applications.

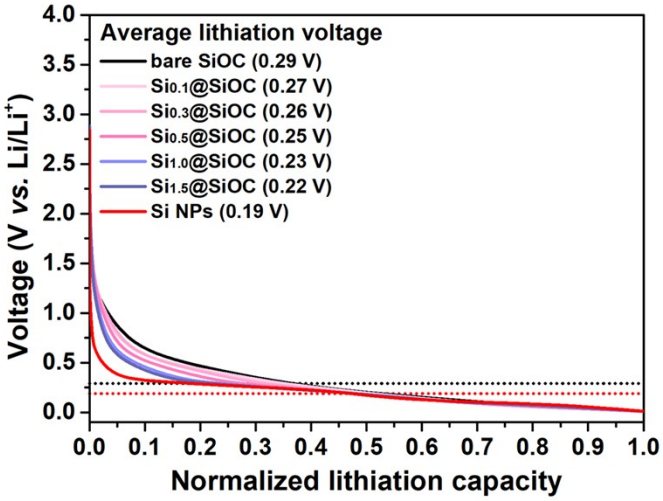

Fig. S7. Normalized lithiation capacity plot of bare SiOC, various Si_x@SiOC, and Si NPs electrodes.

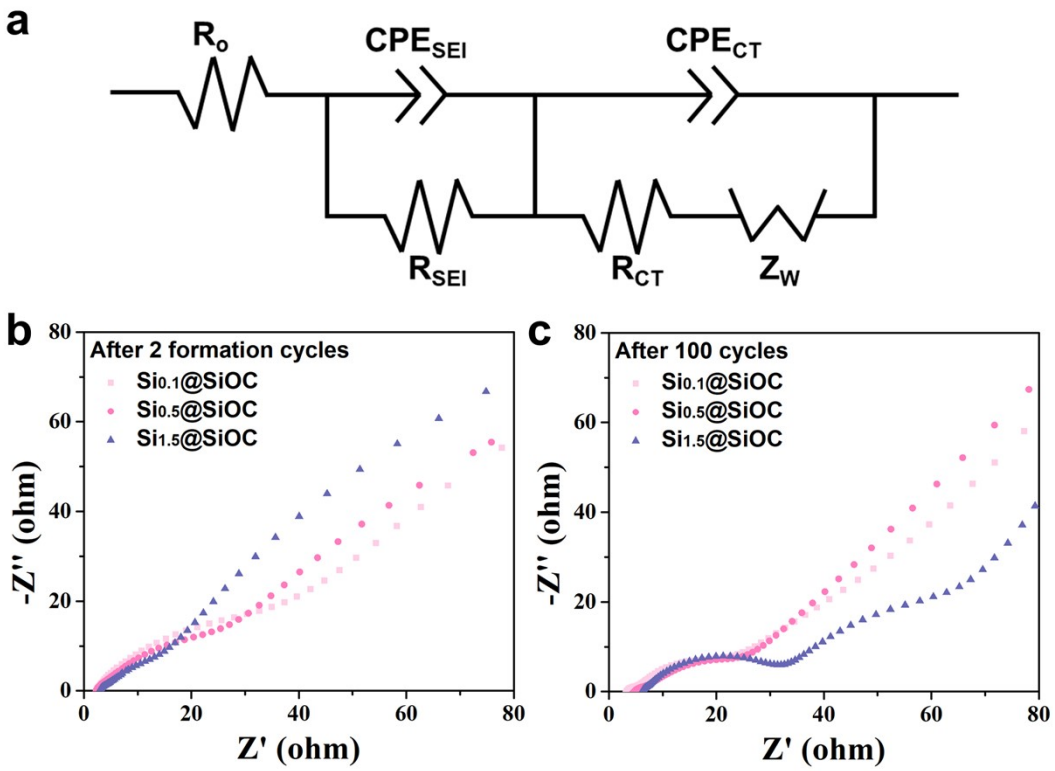

Fig. S8. (a) Equivalent circuit diagram used for fitting the impedance spectra. Nyquist plots of Si_x@SiOC electrodes after (b) formation cycles and (c) 100 cycles.

Fig. S8a displays an equivalent circuit diagram of the Si_x@SiOC electrodes. The circuit model consists of the following impedance factors: the ohmic resistance (R_o) of the electrolyte and electrodes, SEI layer resistance (R_{SEI}), charge transfer resistance (R_{CT}), Warburg diffusion impedance (Z_w), and constant phase elements (CPE_{SEI} and CPE_{CT}). The resistance values obtained from the Nyquist plots are listed in **Table S3**. Electrochemical impedance spectroscopy (EIS) was used to investigate the effect of CAS of Si NPs on the resistance of the composite electrodes. The Nyquist plots of the $Si_{0.1}$@SiOC, $Si_{0.5}$@SiOC, and $Si_{1.5}$@SiOC electrodes after two formation cycles and 100 cycles are shown in **Fig. S8b-c** for comparison with the Si_x@SiOC system. As shown in the Nyquist plots of all electrodes, two suppressed semicircles corresponding to R_{SEI} and R_{CT} were observed. The first semicircle in the high-frequency region represents the R_{SEI} associated with Li ion diffusion through the surface SEI layer [4]. The second semicircle in the middle-frequency region corresponds to the R_{CT} related to the charge transfer reactions at the surface of the active materials [5].

Analyzing and comparing the changes in these resistances between cycles provided detailed insights into the impact of Si-NP seeding on the redox reaction kinetics of Si@SiOC electrodes. From **Fig. S8b**, it is evident that the R_{CT} decreases with an increase in the number of Si NPs embedded in SiOC. The decrease, despite the low electrical conductivity of the Si NPs, is

attributed to the diminished proportion of the bulky SiOC matrix, which results in faster Li-ion diffusion, and thus, higher activation of the electrode at an early stage. After 100 cycles (**Fig. S8c)**, the R_{SEI} and R_{CT} resistances of the $Si_{0.1}$@SiOC and $Si_{0.5}$@SiOC electrodes remained consistent with their initial levels because the SiOC matrix was sufficiently activated and the internal Si NPs were safely protected by the matrix. In contrast, the R_{SEI} and R_{CT} of $Si_{1.5}$@SiOC increased because the structure of the composite collapsed owing to the volumetric changes of the Si NPs during cycling, allowing the SEI layer to propagate through the fractured regions.

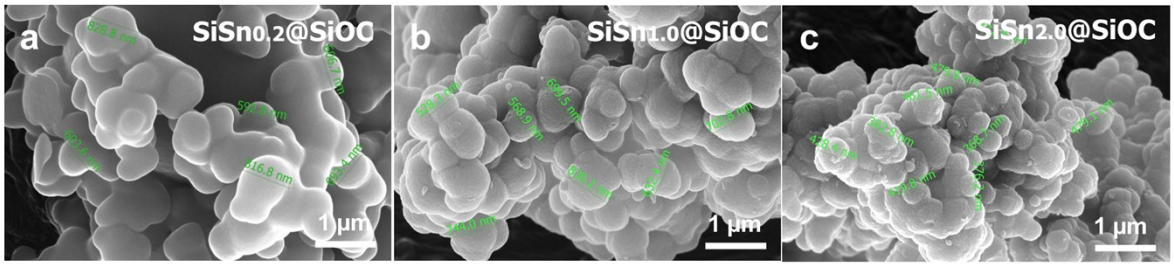

Fig. S9. Powder SEM images of various $SiSn_x$@SiOC composites.

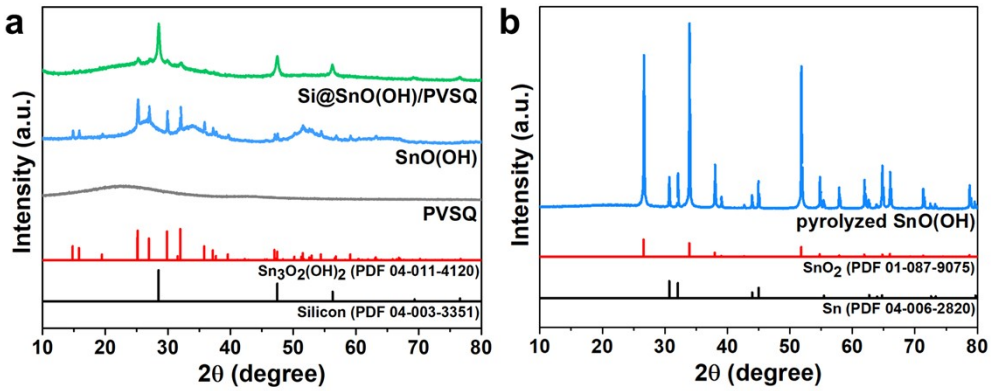

Fig. S10. XRD patterns of (a) Si@SnO(OH)/PVSQ, SnO(OH), PVSQ, and (b) pyrolyzed SnO(OH) samples.

Fig. S10b shows the XRD pattern of the pyrolyzed SnO (OH) sample without Si NPs and PVSQ. The pyrolyzed SnO(OH) samples were composed of Sn and SnO_2, indicating the role of SiOC as a reducing agent during pyrolysis.

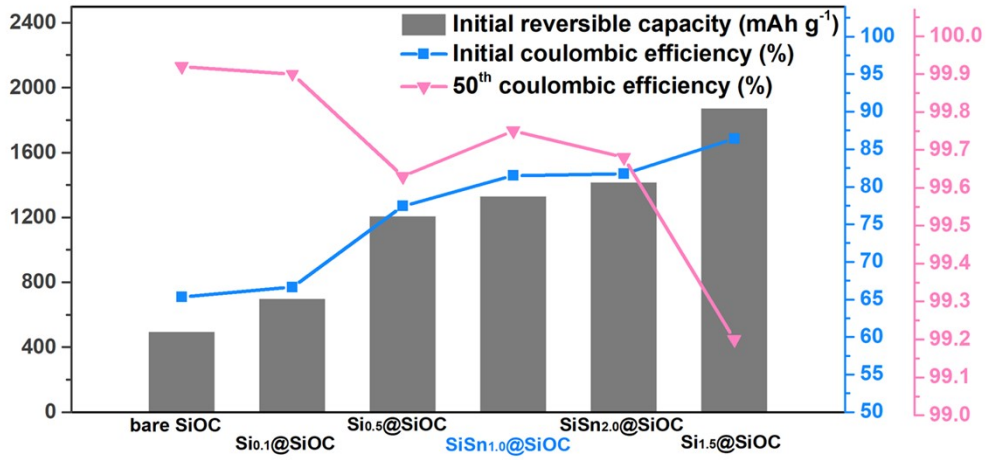

Fig. S11. Comprehensive comparison of anode performances (initial reversible capacity, ICE, and coulombic efficiency of the 50th cycle) between bare SiOC, various Si_x@SiOC and $SiSn_x$@SiOC composites.

$Si_{0.5}$@SiOC, which exhibited the best overall anode performance among Si@SiOC composites, featured a capacity of 1,176 mAh g^{-1}, ICE of 77.4%, and CE of 99.63% at the 50th cycle, signifying cycle stability. It should be noted that comparable attributes were observed in $SiSn_{1.0}$@SiOC, which displayed an overall electrochemical performance improvement with values of 1,329 mAh g^{-1}, ICE of 81.5%, and CE of 99.75% at 50th cycle, respectively. Notably, in the case of $SiSn_{2.0}$@SiOC, which had the highest Sn content, there was only a slight decrease in the 50th Coulombic efficiency (99.68%). This minor decline could be attributed to the volumetric variations experienced by the larger Sn clusters (> 100 nm) during cycling. These results imply that, despite the relatively low Sn within content in the composite (*i.e.*, 0.33~ 2.17 wt.%), the improvements in the overall anode performance can be attributed to Sn's beneficial role played by the dual matrix of Sn/SiOC. The morphological advantages of the Sn/SiOC dual matrix are additionally discussed in the Supporting Information through a variety of analyses, including cross-sectional SEM and electrochemical analyses.

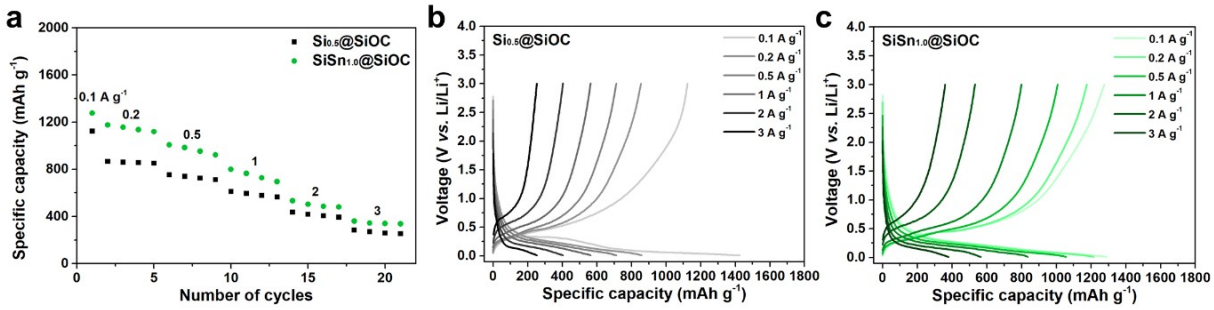

Fig. S12. (a) Specific capacity of Si@SiOC and SiSn@SiOC electrodes at various current densities from 0.1 to 3 A g^{-1}. Galvanostatic charge-discharge curves of (b) Si@SiOC and (c) SiSn@SiOC electrodes at various current densities from 0.1 to 3 A g^{-1}.

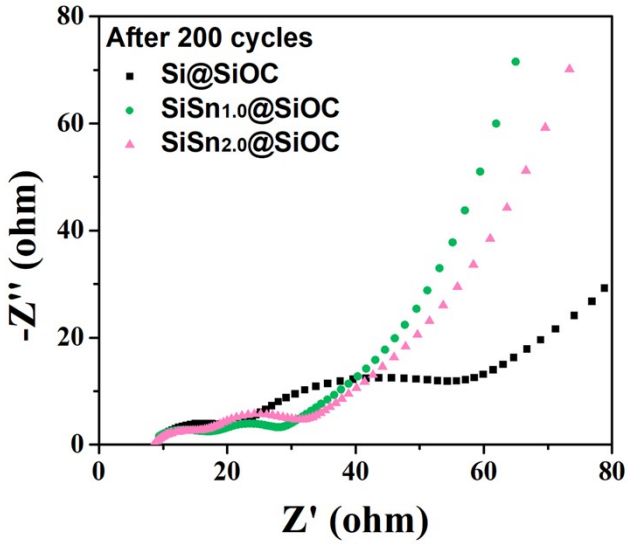

Fig. S13. Nyquist plots of Si@SiOC and $SiSn_x$@SiOC electrodes after 200 cycles.

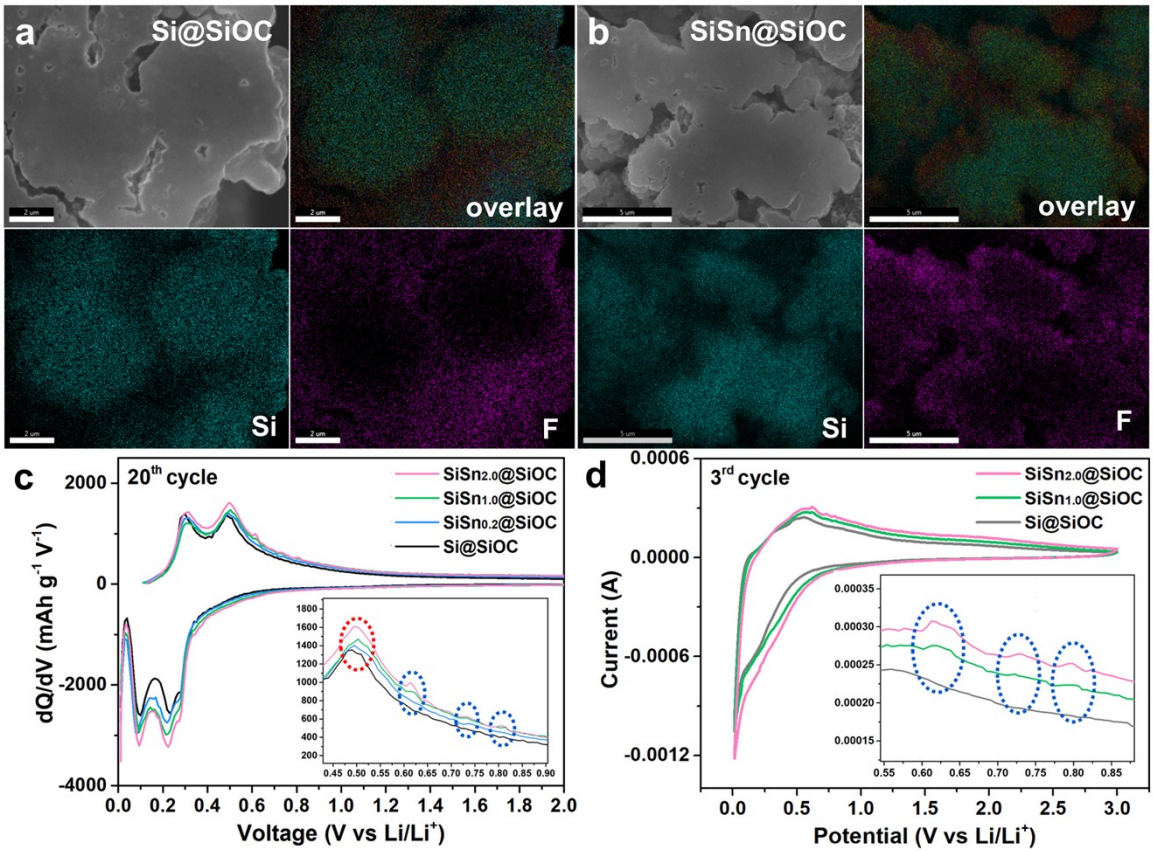

Fig. S14. Cross-sectional SEM image and EDS mapping images of (a) Si@SiOC electrode and (b) SiSn@SiOC electrode after precycling (delithiated states). (c) dQ dV^{-1} plot and (d) CV profiles of Si@SiOC and $SiSn_x$@SiOC electrodes at a scanning rate of 0.05 mV s^{-1}.

To explore the advantages of the Sn/SiOC dual matrix comprehensively, we conducted in-depth investigations (cross-sectional SEM and electrochemical analyses). **Fig. S14a and b** show the cross-sectional SEM image and corresponding EDS mapping data of the Si@SiOC ($Si_{0.5}$@SiOC) and SiSn@SiOC ($SiSn_{1.0}$@SiOC) electrodes obtained by disassembling the coin cell after precycling (20 cycles). The F mapping assisted in detecting the distribution of LiF, an SEI layer component originating from the FEC additive within the electrolyte. Thus, tracing LiF provides visual insight into the electrolyte wetting of the particles after cycling. In the Si@SiOC electrode (**Fig. S14a**), LiF was formed along the surface of Si@SiOC particles, sized between 3 to 7 um. Conversely, in the SiSn@SiOC electrode (**Fig. S14b**), LiF was distributed along the surface of primary particles with a size of less than 1 μm. The inherent voids within the SiSn@SiOC facilitated a larger electrolyte-wetted area compared to Si@SiOC, which is beneficial for a shorter Li-ion pathway to the inner Si NP. The incorporation of Sn into Si@SiOC induces a morphological change in the particles, resulting in the full utilization of the internal Si NPs, optimizing the utilization of the internal Si NPs, and thereby increasing the

specific capacity of the composite. In addition, the electrochemical performance verified that SiSn@SiOC maintained a high coulombic efficiency during cycling because of the electrochemical stability of the SiOC matrix, despite the expanded electrolyte-wetted area.

Differential capacity analysis (dQ/dV) and cyclic voltammetry (CV) of the SiSn@SiOC electrodes were performed to determine the Li-ion activity of the components in the SiSn@SiOC. The dQ/dV curves of the 20th cycle are displayed in **Fig. S14c,** while the CV curves of the 3rd cycle are shown in **Fig. S14d**. In the CV curves of the SiSn@SiOC samples, no characteristics indicative of Li-Sn alloying were observed in the cathodic branches. This is because the reduction reaction of all constituents occurred below 0.5 V, causing peak overlap. However, in the anodic branches of $SiSn_{1.0}$@SiOC and $SiSn_{2.0}$@SiOC, three weak dealloying signals are observed at 0.63, 0.73, and 0.79 V, corresponding to Li_7Sn_3→LiSn, LiSn→Li_2Sn_5, and Li_2Sn_5→Sn, respectively (**Fig. S14d**, blue dotted circles of inset image) [6, 7]. In the dQ/dV curves, three peaks consistent with the dealloying peaks of the CV curves are observed (**Fig. S14c**; blue dotted circles in the inset image), along with the alloying/dealloying peaks of the Si NPs. In particular, the strong Li−Sn dealloying signals in the $SiSn_{2.0}$@SiOC sample suggest that significant mechanical stress was applied to the inside of the particle, where larger groups of Sn over 100 nm are embedded. This is related to the poorer cycle stability of $SiSn_{2.0}$@SiOC compared to those of $SiSn_{0.2}$@SiOC and $SiSn_{1.0}$@SiOC. In the dQ dV^{-1} curves of all samples, Li−Si alloying/dealloying peaks are clearly observed, and each peak shows differences in intensity. The lithiation peaks of Si NPs appear at 0.24−0.29 and 0.09 V, corresponding to the alloying process of a-Si→$Li_{2.0}Si$ and $Li_{2.0}Si$→$Li_{3.5}Si$, respectively. The delithiation peaks of Si NPs appear at 0.25 and 0.5 V, corresponding to the dealloying process of $Li_{3.5}Si$→$Li_{2.0}Si$ and $Li_{2.0}Si$→a-Si (a red dotted circle of inset image), respectively. The intensity of the (de)alloying peaks of the Si NPs increased with increasing Sn content, indicating that one of the reasons for the enhancement in the specific capacity of SiSn@SiOC is the increased utilization of Si NPs. Through these analyses, we demonstrate that the incorporation of Sn facilitates the comprehensive utilization of Si NPs in SiSn@SiOC composites.

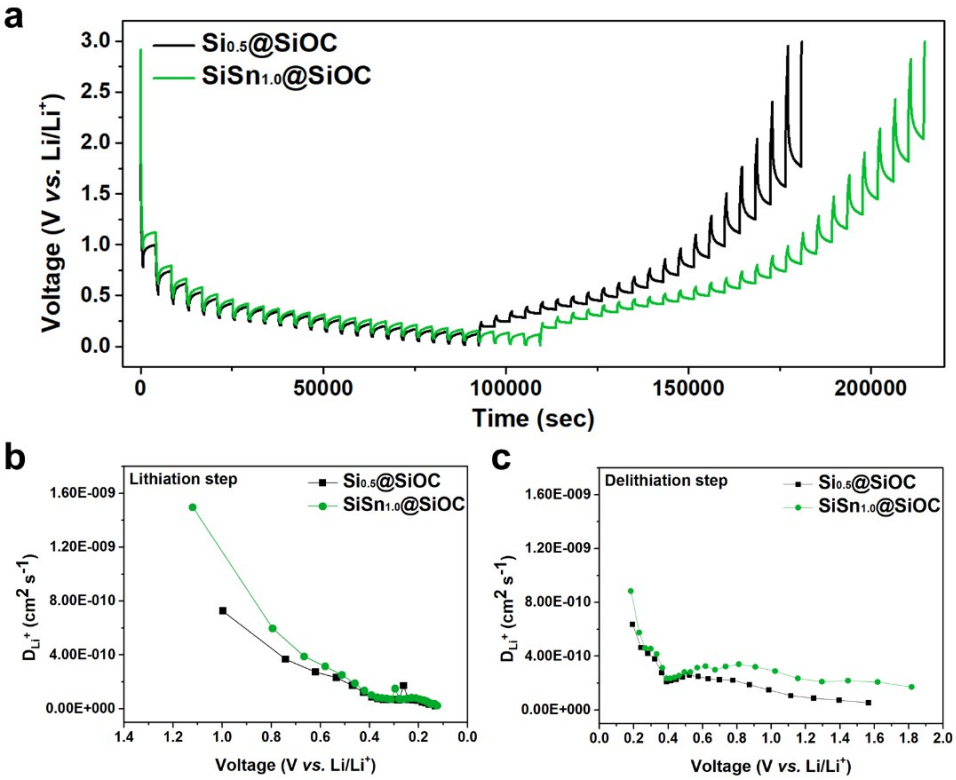

Fig. S15. (a) GITT profiles and (b, c) calculated Li^+ diffusion coefficients of Si@SiOC and SiSn@SiOC electrodes during lithiation and delithiation processes.

References

1. D. A. Loy, B. M. Baugher, C. R. Baugher, D. A. Schneider and K. Rahimian, *Chem. Mater.*, 2000, **12**, 3624-3632.
2. S. Dirè, V. Tagliazucca, E. Callone and A. Quaranta, *Mater. Chem. Phys.*, 2011, **126**, 909-917.
3. M. Wilamowska-Zawlocka, P. Puczkarski, Z. Grabowska, J. Kaspar, M. Graczyk-Zajac, R. Riedel and G. D. Sorarù, *RSC Adv.*, 2016, **6**, 104597-104607.
4. S. S. Zhang, K. Xu and T. Jow, *Electrochim. Acta*, 2006, **51**, 1636-1640.
5. C. Pastor-Fernández, W. D. Widanage, J. Marco, M.-A. Gama-Valdez and G. H. Chouchelamane, 2016.
6. N. Oehl, G. Schmuelling, M. Knipper, R. Kloepsch, T. Placke, J. Kolny-Olesiak, T. Plaggenborg, M. Winter and J. Parisi, *CrystEngComm*, 2015, **17**, 8500-8504.
7. S. Eun Wang, J.-S. Park, M. Ji Kim, Y. Chan Kang and D. Soo Jung, *Appl. Surf. Sci.*, 2022, **589**.